LETTER

Distal Synergistic Effect in Bimetal−Organic Framework for Superior Catalytic Water Oxidation

Umashis Bhoi, Subhasmita Ray, Sujit Bhand, Pranay Ninawe, Debashree Roy, Shammi Rana, Kartick Tarafder, and Nirmalya Ballav*

Read Online

ACCESS | Metrics & More | Article Recommendations | SI Supporting Information

ABSTRACT: Metal−organic frameworks (MOFs) are emerging as promising electro-catalysts for the oxygen evolution reaction (OER). The bimetallic design strategy was further adopted in MOFs to elevate the OER performance by a synergistic effect. The proximal metal−oxygen−metal bonding configuration with typical $3d_{\pi}−2p_{\pi}−3d_{\pi}$ interaction was apparently essential for an effective electronic coupling between the metal centers. Here, we report an example of distal synergy in a bimetal−organic framework exhibiting a better OER activity than the monometallic counterparts, as well as the conventional proximal synergy. To achieve a current density of 10 mA·cm^{-2}, our electrodeposited bimetallic MOF, Co−Ni-$(TCNQ)_2(H_2O)_2$ (TCNQ = 7,7,8,8-tetracyanoquinodimethane), on

a glassy-carbon electrode required an overpotential value of 220 mV. X-ray photoelectron spectroscopy (XPS) and density functional theory (DFT) calculations revealed distinctive electronic coupling between the Co(II)-$3d^7$ and Ni(II)-$3d^8$ centers, despite being 9 Å apart, leading to an overall charge delocalization in the structure via TCNQ.
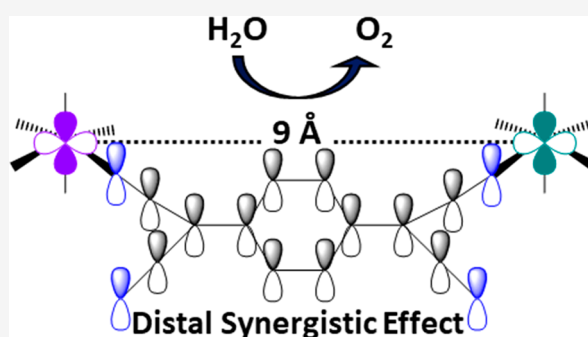
Oxidation of water is considered to be one of the most thermodynamically challenging chemical reactions,[1] and an unprecedented design of nature is the photosystem-II (PSII),[1,2] which is responsible for the conversion of water to molecular oxygen (a four-electron process) with the help of solar energy.[3] A cubane-like Mn_3CaO_4 cluster connected to a fourth Mn center by a mono-μ-oxo bridge has been identified as the oxygen evolution complex (OEC) within PSII.[1,4,5] Subsequently, a lot of effort has been paid to understand the underlying mechanism of photosynthetic water splitting as well as mimicking the process viz. artificial photosynthesis.[2,6−11] Initially, Ca was proposed to play the role of water coordination in the OEC of PSII,[12,13] however, it was understood later that redox-inactive metals like Ca crucially modulates the reduction potential of the redox-active Mn centers via the μ-oxo bridges in the Mn_3CaO_4 cluster.[6] Electronic interaction and/or cooperative effect between metal centers was realized to play an important role in the catalytic cycle,[14,15] and various bimetallic systems started to emerge as superior catalysts for the oxygen evolution reaction (OER)—ranging from nanoparticles,[9,16] oxides,[17−19] perovskites,[20] carbides,[21] coordination complexes,[7,22] and down to metal−organic frameworks (MOFs).[23,24] The versatile chemistry involving MOFs has witnessed a tremen-

dous surge in developing efficient electro-catalysts over the past decade, especially bimetal−organic frameworks for improvising the OER activity.[25,26] An archetypical example is the bimetallic Ni−Co-MOF exhibiting superior OER performance compared to the respective monometallic counterparts which have been assigned to be due to the efficient electronic coupling between Ni and Co centers via O; precisely, $d_{\pi}−p_{\pi}$ electron donation in the Co−O−Co configuration and $d_{\pi}−p_{\pi}$ electron repulsion in the Ni−O−Ni configuration are duly optimized in the Co−O−Ni configuration.[27]

The metal centers are usually connected via O in bimetallic MOFs showing OER activity,[27−31] and the average metal-to-metal nearest distance was found to be ~3 Å, a signature of strong electronic coupling via chemical bonds.[27] Therefore, the so-called "synergistic effect" in bimetallic systems directly reflects the "proximity"[27] influence and "distal synergy"
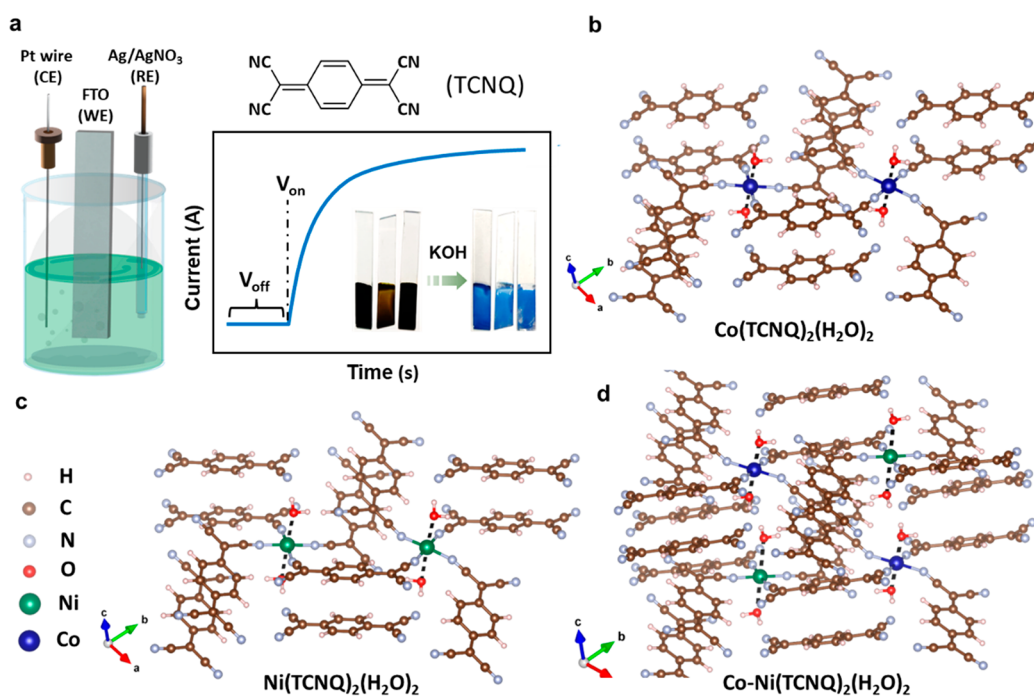
Figure 1. Schematics of electrocrystallization and crystal structures. (a) Schematic depicting the three-electrode setup used for electrocrystallization of $M(TCNQ)_2$ onto the FTO substrate along with the pictorial representation of the current profile during the electrocrystallization. Energy optimized crystal structures obtained via DFT calculations for (b) $Co(TCNQ)_2(H_2O)_2$, (c) $Ni(TCNQ)_2(H_2O)_2$, and (d) $Co-Ni(TCNQ)_2(H_2O)_2$.

remained elusive in the domain of electro-catalysis, specifically oxidation of water. Herein, we report a distal synergistic effect (∼9 Å) for the OER activity in a bimetallic MOF comprised of Co(II) ($3d^7$) and Ni(II) ($3d^8$) metal centers and TCNQ ligand. The electrocrystallized bimetallic $Co-Ni(TCNQ)_2$ exhibited superior OER performance compared to monometallic $Co(TCNQ)_2$ and $Ni(TCNQ)_2$ counterparts, further surpassing the overpotential value achieved earlier[27] with the bimetallic Ni-Co-BDC (BDC = benzene dicarboxylic acid) MOF bearing the proximal Co-O-Ni synergy. Within the proton-coupled electron transfer (PCET) mechanistic pathway,[3] estimation of the Gibbs free energy by density functional theory (DFT) calculations for the bimetallic $Co-Ni(TCNQ)_2$ system was observed to be significantly lower than those of the monometallic $Co(TCNQ)_2$ and $Ni(TCNQ)_2$ systems, thereby complementing the experimental results. Such a distal synergy is understood to be due to subtle yet distinctive charge-transfer between the Co(II) and Ni(II) centers and/or electron delocalization involving the TCNQ ligand, as was evident from the overlap of the density of states (DOS) of the respective $3d$ orbitals near the Fermi (E_F) level. This work undoubtedly highlights the fact that in catalysis an efficient electronic coupling between the active metal centers (orbitals energy and occupancy) is more important in bimetallic synergy than their spatial arrangement and/or the proximity effect.

Using an electrocrystallization technique, monometallic ($Co(TCNQ)_2$ and $Ni(TCNQ)_2$) and bimetallic ($Co-Ni(TCNQ)_2$) thin films were deposited on a fluorine-doped tin oxide (FTO) substrate. A three-electrode system was used, with the FTO as the working electrode and platinum and Ag/AgNO_3 as counter and reference electrodes, respectively (Figures 1a and S1). The three-electrode setup was dipped in an electrochemical cell containing a mixture of metal salt(s) ($Co(NO_3)_2 \cdot 6(H_2O)$) and/or $Ni(NO_3)_2 \cdot 6(H_2O)$), TCNQ,

and tetrabutylammonium perchlorate (TBAP) electrolyte in acetonitrile solvent. A constant electrical potential (−0.5 V) was applied, resulting in an increase of current followed by saturation due to the deposition of material on the electrode surface as indicated by the visible color change (Figure 1a). The electrodeposited thin films were thoroughly washed with acetonitrile and dried at room temperature. As-deposited films were found to be highly crystalline and the out-of-plane X-ray diffraction (XRD) patterns suggested that $Co(TCNQ)_2$ and $Ni(TCNQ)_2$ are isostructural;[32] hence, the bimetallic $Co-Ni(TCNQ)_2$ also exhibited a similar diffraction pattern (Figure S2). The specific XRD peaks (less in number compared to the simulated pattern) present in $Co(TCNQ)_2$, $Ni(TCNQ)_2$, and $Co-Ni(TCNQ)_2$ are possibly due to the oriented growth and may also affect the relative intensities upon changing the metal ion. The local chemical bonding scenario in the bimetallic $Co-Ni(TCNQ)_2$ thin film was investigated by Raman spectroscopy. TCNQ being a redox-active molecule exists in three forms: neutral, monoanionic, and dianion.[33] The neutral TCNQ ligand showed four intense Raman bands at ∼1204 cm^{-1}, ∼1451 cm^{-1}, ∼1599 cm^{-1}, and ∼2224 cm^{-1} corresponding to C=C-H bending, C-CN stretching, C=C ring stretching, and CN stretching modes, respectively.[34] In both monometallic and bimetallic thin films, the peak corresponding to C-CN stretching shifted to a lower wavenumber at ∼1387 cm^{-1}, indicating the coordination of the TCNQ ligand to the Co/Ni center and the existence of TCNQ in radical-anion form (Figure S3). A shoulder peak appeared around ∼1320 cm^{-1}, a signature of dianion ionic TCNQ, along with the minor shift and broadening of the peak corresponding to ∼CN stretching (∼2220 cm^{-1}), indicative of the disproportionation of a small amount of TCNQ radical-anion into neutral TCNQ and dianionic TCNQ (Figure S3). Field-emission scanning electron microscopy (FESEM) images endorsed the formation
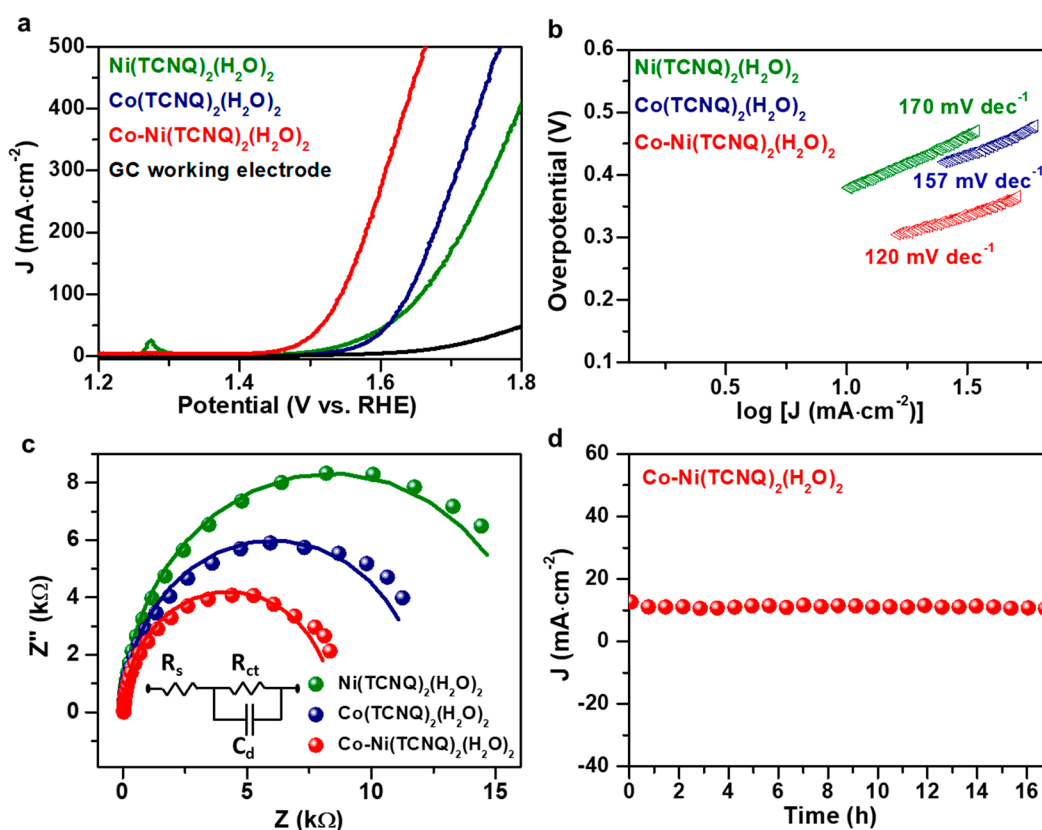
Figure 2. Electrochemical study. (a) Linear sweep voltammetry (LSV) curves recorded at a scan rate of 10 mV·s^{-1}. (b) Tafel plots with respective Tafel slope values. (c) Nyquist plots for Co(TCNQ)$_2$(H$_2$O)$_2$, Ni(TCNQ)$_2$(H$_2$O)$_2$, and Co−Ni(TCNQ)$_2$(H$_2$O)$_2$ (inset: equivalent circuit). (d) Electrochemical durability evaluated at a constant applied potential of 220 mV in Co−Ni(TCNQ)$_2$(H$_2$O)$_2$.

of highly uniform thin films for both monometallic and bimetallic systems with an average thickness value of ∼1.5 μm (Figure S4−5). The elemental mapping by energy-dispersive X-ray spectroscopy (EDXS) clearly revealed the uniform presence of Co and Ni in the bimetallic Co−Ni(TCNQ)$_2$ thin film with the Co-to-Ni atomic ratio of ∼1:1 (Figures S6 and S7). The EDXS spectra on the bimetallic thin film also displayed the characteristic Co L_α line and Ni L_α line at ∼0.75 eV and ∼0.85 eV, respectively, which matched well with those for the monometallic thin films (Figure S7).

In view of studying the OER activity in the alkaline medium, the electrodeposited thin films on FTO substrate were immersed in 1 M KOH solution, and interestingly, a distinct color change was observed in all the samples which could be due to change in the coordination environment of the metal ions, viz. structure (Figure 1a). The XRD pattern was found to be noticeably different compared to the pristine samples and matched well with that of the Mn(TCNQ)$_2$(H$_2$O)$_2$ system, where the major diffraction peaks were observed at 2θ values of ∼14, ∼15.5, ∼19, and ∼20 corresponding to 200, 12$\bar{1}$, 20$\bar{2}$, and 202 planes (Figure S2).[35] Therefore, the changes in the XRD pattern can be ascribed to be due to the structural change via the coordination of two water molecules in the axial positions for Ni and Co in both monometallic Co(TCNQ)$_2$ and Ni(TCNQ)$_2$ and bimetallic Co−Ni(TCNQ)$_2$, leading to the formation of Co(TCNQ)$_2$(H$_2$O)$_2$, Ni(TCNQ)$_2$(H$_2$O)$_2$, and Co−Ni(TCNQ)$_2$(H$_2$O)$_2$, respectively. The Fourier-transformed infrared (FTIR) spectra further confirmed the binding of H$_2$O molecules as the broad OH stretching peak appeared in Co−Ni(TCNQ)$_2$(H$_2$O)$_2$, which was absent in Co−

Ni(TCNQ)$_2$ (Figure S8). Moreover, X-ray photoelectron spectroscopy (XPS) data clearly showed the presence of strong satellite signal in the case of Ni 2p photoemission of the Co−Ni(TCNQ)$_2$(H$_2$O)$_2$ system, indicating the presence of Ni(II) ions in high-spin octahedral geometry with two H$_2$O molecules located at the axial positions, instead of a square-planar/tetrahedral geometry, with no unpaired electrons and would not result in such strong satellite signal, as observed in the Ni 2p photoemission of the Co−Ni(TCNQ)$_2$ system (Figure S9).[36]

The initial geometry of the Co(TCNQ)$_2$(H$_2$O)$_2$ and Ni(TCNQ)$_2$(H$_2$O)$_2$ unit cells were constructed from the known crystal structure of Mn(TCNQ)$_2$(H$_2$O)$_2$, in which Mn(II) ions were replaced with either Co(II) or Ni(II) ion and then the energy-optimized ground-state geometries were obtained by performing the density functional theory (DFT) calculations (Figures 1b-d and S10−S12).[37−39] As for the bimetallic Co−Ni(TCNQ)$_2$(H$_2$O)$_2$ system, stoichiometric Co(II) and Ni(II) ions were used in place of Mn(II) ions in the nearest neighbor configuration (Figures 1d and S12). The Co−O bond distance was found to be slightly smaller compared to the Ni−O bond distance in Co(TCNQ)$_2$(H$_2$O)$_2$ and Ni(TCNQ)$_2$(H$_2$O)$_2$, as well as in Co−Ni(TCNQ)$_2$(H$_2$O)$_2$ (Figures 1b−d and S10−S13). FESEM images revealed rod-like morphology in hydrated samples, markedly different from the pristine samples, though the Co:Ni ratio was unchanged as observed from the EDXS analyses along with a uniform distribution of Co and Ni across the sample (Figures S5−S7). Raman spectra for Co-(TCNQ)$_2$(H$_2$O)$_2$, Ni(TCNQ)$_2$(H$_2$O)$_2$, and Co−Ni-
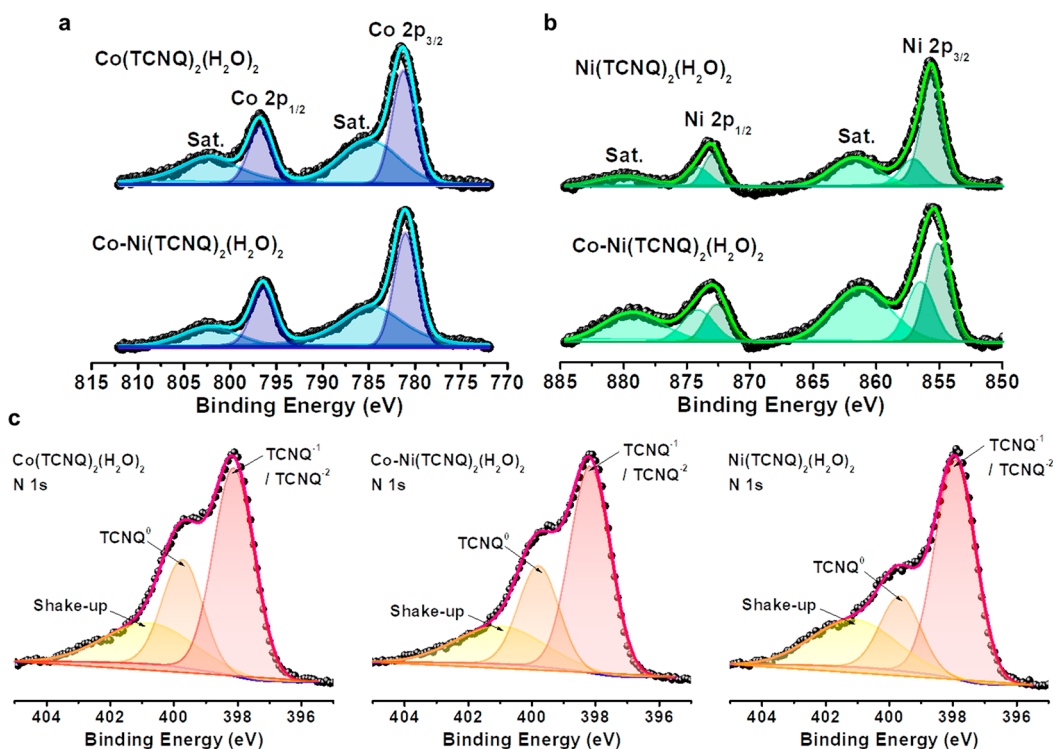
Figure 3. X-ray photoelectron spectroscopy. (a) Co 2p and **(b)** Ni 2p XPS spectra depicting the $2p_{1/2}$ and $2p_{3/2}$ signals along with the respective satellite signals; **(c)** N 1s XPS spectra with the deconvoluted signals for $TCNQ^0$ and $TCNQ^{-1}/TCNQ^{-2}$.

$(TCNQ)_2(H_2O)_2$ were observed to be similar to those of respective pristine samples, without any significant change in the peak position, implying that the bonding scenario of the TCNQ ligand with metal ions was unaltered (Figure S3).

The monometallic $Co(TCNQ)_2(H_2O)_2$ and $Ni-(TCNQ)_2(H_2O)_2)$ and bimetallic $Co-Ni(TCNQ)_2(H_2O)_2$ were electrodeposited onto the glassy-carbon (GC) electrode, and respective OER performances were evaluated. Our approach of electrocrystallization for the direct growth of the catalyst on the electrode surface is certainly advantageous over the conventional drop casting method, giving rise to better charge-transfer between the electrode and active material, in turn influencing the catalytic performance. All electrochemical measurements were carried out in the conventional three-electrode configuration in 1 M KOH solution. Linear sweep voltammetry (LSV) was employed to obtain the polarization curves (Figure 2a). The evolution of the O_2 gas was also visualized on the GC electrode during the measurements. E_{onset} and $E_{j=10}$ (overpotential value at 10 mA·cm^{-2}) are usually the key parameters to assess the OER performance.[27] The bimetallic $Co-Ni(TCNQ)_2(H_2O)_2$ displayed a lower onset potential of ∼1.45 V, where the thermodynamic OER potential is $E^0H_2O/O_2 = $ ∼1.23 V. At a current density of 10 mA·cm^{-2}, the overpotential value of 220 mV for the bimetallic $Co-Ni(TCNQ)_2(H_2O)_2$ system was significantly lower than the overpotential values of 280 and 310 mV for the monometallic $Ni(TCNQ)_2(H_2O)_2$ and $Co(TCNQ)_2(H_2O)_2$ systems, respectively (Figures 2a and S14). Notably, the overpotential value of our bimetallic $Co-Ni(TCNQ)_2(H_2O)_2$ is superior to that of the earlier reported bimetallic Co-Ni-MOFs[27] for the OER activity and also stood out when compared to other TCNQ-based MOFs[40−47] (Table S1) as well as other bimetallic MOFs in general (Table S2).[27−31,48,49]

The kinetic aspect of the OER catalysis was evaluated from the Tafel plots, and the estimated slope value of 120 mV·dec^{-1} for the bimetallic $Co-Ni(TCNQ)_2(H_2O)_2$ was found to be significantly smaller than those of monometallic $Co-(TCNQ)_2(H_2O)_2$ (157 mV·dec^{-1}) and $Ni(TCNQ)_2(H_2O)_2$ (170 mV·dec^{-1}), indicating faster reaction kinetics in the former system (Figure 2b).[50] The Tafel slope values complemented the overpotential values obtained from the LSV curves: bimetallic is better than monometallic. Electrochemical impedance spectroscopy (EIS) analyses (Nyquist plots; fitted with Randles equivalent circuit) suggested a smaller charge-transfer resistance (R_{ct} ≈ 8 kΩ) for the bimetallic $Co-Ni(TCNQ)_2(H_2O)_2$, as compared to those of $Co(TCNQ)_2(H_2O)_2$ (R_{ct} ≈ 13 kΩ) and $Ni(TCNQ)_2(H_2O)_2$ (R_{ct} ≈ 18 kΩ), indicative of a faster electron transfer across the electrode−electrolyte interface (Figure 2c). The electrochemical durability was tested upon applying a constant applied potential of 220 mV and measuring the current density value for ∼17 h; remarkably, it was found to be almost unaltered (∼10 mA·cm^{-2}), which is desired for large-scale electrochemical applications[51] (Figure 2d). Overall, $Co-Ni(TCNQ)_2(H_2O)_2$ outperformed $Co(TCNQ)_2(H_2O)_2$ and $Ni(TCNQ)_2(H_2O)_2$ in the OER activity and clearly reflected a $3d^7-3d^8$ synergistic effect in the bimetallic system.

XPS was employed to probe the electronic interaction between Co, Ni, and TCNQ in $Co(TCNQ)_2(H_2O)_2$, $Ni(TCNQ)_2(H_2O)_2$, and $Co-Ni(TCNQ)_2(H_2O)_2$ (Figure 3). The Co 2p XPS spectra unveiled characteristic signals for the Co $2p_{3/2}$ and $2p_{1/2}$ along with the satellite features; while the spectral signature was mostly retained in the $Co-Ni(TCNQ)_2(H_2O)_2$, a shift of ∼0.4 eV was observed toward the lower binding energy with a noticeable decrease in the satellite intensity, which could be due to the presence of mixed valence states of Co (I/II) (Figure 3a). In the case of Ni 2p
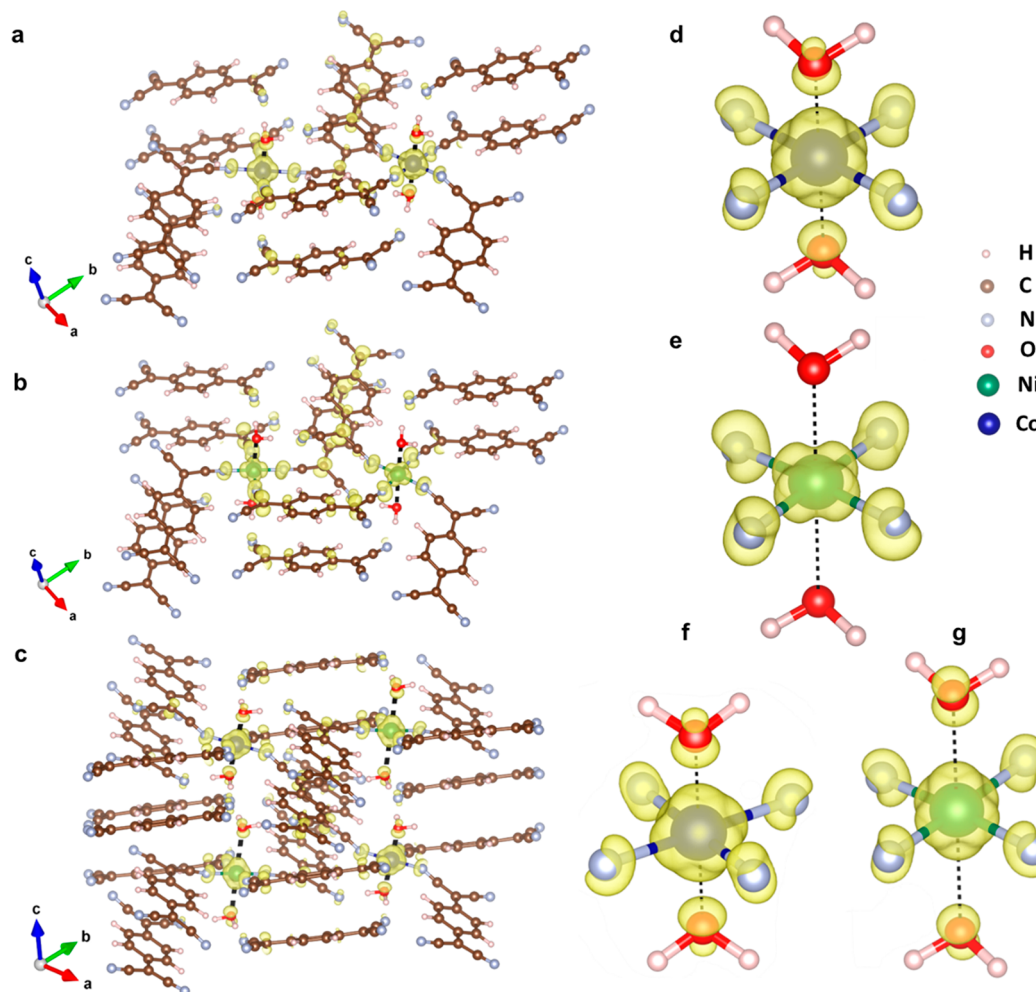
Figure 4. Visualizing the charge distribution. Total charge density plot depicting the electron density across the structure for (a) $Co(TCNQ)_2(H_2O)_2$, (b) $Ni(TCNQ)_2(H_2O)_2$, and (c) $Co-Ni(TCNQ)_2(H_2O)_2$. Zoomed-in charge density plots depicting the electron density in the local structure around (d) Co in $Co(TCNQ)_2(H_2O)_2$, (e) Ni in $Ni(TCNQ)_2(H_2O)_2$, and (f and g) Co and Ni in $Co-Ni(TCNQ)_2(H_2O)_2$.

XPS spectra, a dramatic change (shift and broadening of Ni $2p_{3/2}$ and $2p_{1/2}$ signal) was observed in the Co−Ni-$(TCNQ)_2(H_2O)_2$ as compared to $Ni(TCNQ)_2(H_2O)_2$ (Figure 3b). The deconvoluted signals showed that Ni ions were mostly present as Ni(II) with a minor amount of Ni(III) in the case of monometallic $Ni(TCNQ)_2(H_2O)_2$, whereas in bimetallic Co−Ni$(TCNQ)_2(H_2O)_2$, the amount of Ni(III) was significantly increased (Figure 3b). To understand the charge transfer between the metal centers Co and Ni located ∼9 Å apart, we recorded the N 1s XPS spectra, which indicated the presence of TCNQ in mixed-redox forms, as previously suggested by the Raman spectroscopy. In general, a relatively high disproportionation ($TCNQ^{-1} \rightarrow TCNQ^0 + TCNQ^{-2}$) was observed in $Ni(TCNQ)_2(H_2O)_2$ as compared to Co-$(TCNQ)_2(H_2O)_2$, possibly due to the higher redox activity of Ni as compared to Co (Figures 3c and S15). Ideally, the N 1s XPS spectral feature of Co−Ni$(TCNQ)_2(H_2O)_2$ contains a 1:1 ratio of Co: Ni and should be the average of the two $Co(TCNQ)_2(H_2O)_2$ and $Ni(TCNQ)_2(H_2O)_2$; however, we observed that the spectral feature resembles more of the signal from $Co(TCNQ)_2(H_2O)_2$, which indicated charge transfer and/or electron delocalization between Co and Ni ions via TCNQ in the bimetallic system (Figure 3c). A similar charge-transfer and/or electronic coupling was also attributed to the

bimetallic Co−Ni-MOF where metal centers Co and Ni were ∼3 Å apart.[27]

To gain detailed insight into the charge-transfer and/or electron delocalization mechanism, the total charge density plots were extracted from the energy-optimized structures of $Co(TCNQ)_2(H_2O)_2$, $Ni(TCNQ)_2(H_2O)_2$, and Co−Ni-$(TCNQ)_2(H_2O)_2$ (Figures 4 and S16). The electron charge density was majorly located on the Co, Ni, N, and O atoms, with minor density on the C atoms. In $Co(TCNQ)_2(H_2O)_2$, a uniform distribution of electron density in the equatorial direction (Co−N bonds) and the axial direction (Co−O bonds) was realized (Figures 4a and S16). However, in $Ni(TCNQ)_2(H_2O)_2$, the electron density was majorly present along the equatorial direction (Ni−N bonds), with a negligible amount in the axial direction (Ni−O bonds) complementing the longer Ni−O bond (2.57 Å) compared to the Co−O bond (1.97 Å) (Figures 4a,b and S16). In the Co−Ni-$(TCNQ)_2(H_2O)_2$ system, the electron density around Co was observed to be similar to that of the $Co(TCNQ)_2(H_2O)_2$. Interestingly, however, the electron density around Ni in the Co−Ni$(TCNQ)_2(H_2O)_2$ system was markedly different from that of the $Ni(TCNQ)_2(H_2O)_2$, specifically electron density along the axial (Ni−O bonds) and equatorial direction (Ni−N bonds) and accumulation of electrons around O. Also, in the

bimetallic system, Co—O and Ni—O bond lengths were found to be 1.96 and 2.68 Å, respectively—shortened and enlarged compared to respective monometallic systems (Figures 4c and S13). The redistributed charge density along Ni—O bonds could be due to the charge-transfer between Ni and Co ions via TCNQ, as indicated by the XPS data, ultimately resulting in superior OER performance by the bimetallic Co−Ni-$(TCNQ)_2(H_2O)_2$ system.

Now, the question arises: what are the charge-transfer and/or electron delocalization paths? To answer this, we have critically examined the total and partial density of states (DOS/PDOS) plots for determining the exact electronic structure, orbital contributions of individual atoms, and overlap of orbitals, giving rise to the overall charge density plots. The respective Co and Ni 3d-orbitals majorly contribute to the valence band maxima in $Co(TCNQ)_2(H_2O)_2$ and Ni-$(TCNQ)_2(H_2O)_2$, whereas a combination of Ni and Co 3d-orbitals build up the valence band maxima in Co−Ni-$(TCNQ)_2(H_2O)_2$; the conduction band minima for both monometallic and bimetallic systems are mainly composed of contributions from N, C, and O orbitals of TCNQ (Figure S17). The salient features of DOS/PDOS can be summarized as follows: (i) Co 3d-states (d_{xy}, d_{yz}, d_{xz}, $d_{x^2-y^2}$, and d_{z^2}) at 0.2 and 0.4 eV in monometallic $Co(TCNQ)_2(H_2O)_2$ are redistributed to 3d-states at 0.2 eV (d_{xy}, d_{xz}, and $d_{x^2-y^2}$) and 0.5 eV (d_{z^2} and d_{yz}) in bimetallic Co−Ni$(TCNQ)_2(H_2O)_2$; (ii) Ni 3d-state (d_{xy}, d_{xz}, and $d_{x^2-y^2}$) at 0.2 eV in monometallic $Ni(TCNQ)_2(H_2O)_2$ is shifted to a lower-energy 3d-state at 0.35 eV (d_{xy}, d_{xz}, and $d_{x^2-y^2}$) in bimetallic Co−Ni-$(TCNQ)_2(H_2O)_2$; (iii) emergence of a new low-density overlapped d-state (3d_{xy} of Co and 3d_{xy} of Ni) at 0.7 eV in bimetallic Co−Ni$(TCNQ)_2(H_2O)_2$; and (iv) emergence of a new high-density Ni 3d-state (d_{z^2} and d_{yz}) at 1.15 eV in bimetallic Co−Ni$(TCNQ)_2(H_2O)_2$. Such a noticeable change in the DOS/PDOS plots suggested an efficient overlap of 3d orbitals of Co and Ni, possibly via π-orbitals of TCNQ in bimetallic Co−Ni$(TCNQ)_2(H_2O)_2$, even though Co and Ni centers are ~9 Å apart (Figures S17−S30).

In an alkaline medium, OER is believed to follow the proton-coupled electron transfer (PCET) pathway which consists of a five-step cycling process starting from the binding of H_2O to the active site via oxidative addition up to the release of O_2 by reductive elimination (Figure 5a).[3] Notably, our $Co(TCNQ)_2(H_2O)_2$, $Ni(TCNQ)_2(H_2O)_2$, and Co−Ni$(TCNQ)_2(H_2O)_2$ could behave as pre-OER redox[3] systems in the OER cycle. We have performed DFT calculations[52] to estimate the Gibbs free energy associated with each OER step upon considering Co as an active site in $Co(TCNQ)_2(H_2O)_2$, while Ni in $Ni(TCNQ)_2(H_2O)_2$, and both Co and Ni in Co−Ni$(TCNQ)_2(H_2O)_2$ (Figures 5b and S31). The Gibbs free energy (ΔG) for each step ultimately showed the ease of reactivity and reaction feasibility: in general, for all three systems, the Gibbs free energy value was found to be positive for steps i, ii, and iv as they are endothermic reactions, while for step iii, the Gibbs free energy value was found to be negative, indicating an exothermic reaction. The total ΔG value was found to be positive; hence, the reaction is feasible only when an external potential is applied (Figures 5b and S31). Further, the overall ΔG value for the bimetallic Co−Ni$(TCNQ)_2(H_2O)_2$ was estimated to be significantly smaller than the ΔG values for the monometallic $Co(TCNQ)_2(H_2O)_2$ and $Ni(TCNQ)_2(H_2O)_2$. Finally, in the bimetallic Co−Ni$(TCNQ)_2(H_2O)_2$, both Co and Ni sites exhibited better
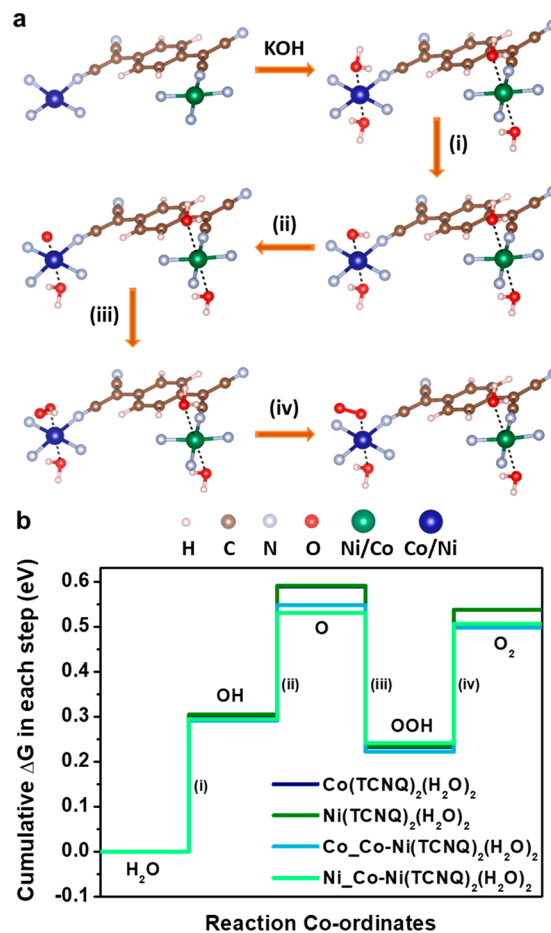

Figure 5. Mechanistic insights of OER by DFT. (a) Insights into the energy-optimized crystal structure of the catalytically active sites for each step in the OER process following the PCET pathway for Co−Ni$(TCNQ)_2(H_2O)_2$. (b) Gibbs free energy plot depicting the cumulative ΔG for each step in the reaction path of the OER considering Co as an active site in $Co(TCNQ)_2(H_2O)_2$, Ni as an active site in $Ni(TCNQ)_2(H_2O)_2$, and Co and Ni as active sites in Co−Ni$(TCNQ)_2(H_2O)_2$.

OER performance compared to their respective monometallic counterparts, with Co slightly outperforming Ni, and therefore strongly supporting the experimental results as well as establishing the distal synergy effect (Figures 5b and S32−S35).

MOFs along with metal chalcogenides, nitrides, and phosphides are known to be prone to electrochemical instability under high-voltage and alkaline conditions, specifically during electro-catalysis in the form of OER.[53−55] Therefore, to rule out the possibility of the conversion of Co−Ni$(TCNQ)_2(H_2O)_2$ to its respective metal (Co/Ni)-oxides/hydroxides, thorough PXRD analysis was carried out, which conclusively dismissed the formation of CoO, NiO, Co_3O_4, $Co(OH)_2$, and $Ni(OH)_2$ (Figure S36). Also, the structural integrity of our bimetallic Co−Ni$(TCNQ)_2(H_2O)_2$ system was found to be intact, after being subjected to multiple OER cycles as evidenced in experimental data presented in Figures S37 and S38: almost identical PXRD patterns, Raman spectra, and FTIR spectra were noted (Figure S37). Additionally, we compared the raw XPS spectral data of the Co−Ni$(TCNQ)_2(H_2O)_2$ sample before and after the OER cycles, and similar spectral features were obtained, unlike chemical

transformation of the catalyst during OER cycles,[56] further complementing the stability of the electronic structure (Figure S38). Finally, upon employing slightly modified reported protocols,[35] we have synthesized bulk (powder) Co-$(TCNQ)_2(H_2O)_2$, $Ni(TCNQ)_2(H_2O)_2$, and Co−Ni-$(TCNQ)_2(H_2O)_2$ samples, and the PXRD patterns matched very well with the respective thin films (Figure S39). In view of the retention of structural integrity, similar physical properties in thin-film configurations is anticipated. The porosity of the powder samples was investigated by studying the N_2 gas sorption isotherms (Figure S39). The BET (Brunauer−Emmett−Teller) surface area values were estimated to be in a similar range: ∼14.5, ∼8.9, and ∼16 $m^2 \cdot g^{-1}$ for Co-$(TCNQ)_2(H_2O)_2$, $Ni(TCNQ)_2(H_2O)_2$, and Co−Ni-$(TCNQ)_2(H_2O)_2$ samples, respectively. Therefore, the better OER performance of the bimetallic Co−Ni$(TCNQ)_2(H_2O)_2$ system as compared to the monometallic Co$(TCNQ)_2(H_2O)_2$, and $Ni(TCNQ)_2(H_2O)_2$ systems is primarily of electronic origin and not directly related to the respective porosity values.

In summary, we have successfully deposited thin films of a bimetal−organic framework, namely, Co−Ni$(TCNQ)_2$, by the electrocrystallization method and subjected to electro-catalysis in the form of the OER activity in an alkaline medium. Among hydrated systems, Co−Ni$(TCNQ)_2(H_2O)_2$ outperformed monometallic Co$(TCNQ)_2(H_2O)_2$ as well as Ni-$(TCNQ)_2(H_2O)_2$. Unlike the conventional bimetallic proximal synergy effect (3 Å), our work demonstrates an example of a distal synergistic effect in electrocatalytic oxidation of water; the nearest distance between Co and Ni active centers is noticeably large (9 Å) in the Co−Ni$(TCNQ)_2$ system. Electronic density of states, as revealed by DFT calculations, evidenced an effective $3d^7$−$3d^8$ electronic coupling, as well as the estimation of Gibbs free energy complementing the experimental results. Such distal synergy resembles enzymatic systems, and upon further tuning of the organic ligand, for example with inductive push−pull effect by suitable substitutions, active metal centers in MOF-based systems are certainly envisioned to show even superior performance in electro-catalysis, including the OER activity.

■ ASSOCIATED CONTENT

Ⓢ Supporting Information

The Supporting Information is available free of charge at https://pubs.acs.org/doi/10.1021/acsenergylett.3c01626.

> Experimental section, theoretical section, PXRD patterns, Raman spectra, FTIR spectra, FESEM images, EDXS analysis, structural information, DOS plots, Gibbs free energy analysis, XPS spectra, gas adsoprtion studies, and stability studies (PDF)

■ AUTHOR INFORMATION

Corresponding Author

Nirmalya Ballav − *Department of Chemistry, Indian Institute of Science Education and Research, Pune 411 008, India;* ⓞ orcid.org/0000-0002-7916-7334; Email: nballav@iiserpune.ac.in

Authors

Umashis Bhoi − *Department of Chemistry, Indian Institute of Science Education and Research, Pune 411 008, India*

Subhasmita Ray − *Department of Physics, National Institute of Technology Karnataka, Mangalore 575 025, India*

Sujit Bhand − *Department of Chemistry, Indian Institute of Science Education and Research, Pune 411 008, India*

Pranay Ninawe − *Department of Chemistry, Indian Institute of Science Education and Research, Pune 411 008, India;* ⓞ orcid.org/0000-0002-8306-9913

Debashree Roy − *Department of Chemistry, Indian Institute of Science Education and Research, Pune 411 008, India*

Shammi Rana − *Department of Chemistry, Indian Institute of Science Education and Research, Pune 411 008, India*

Kartick Tarafder − *Department of Physics, National Institute of Technology Karnataka, Mangalore 575 025, India;* ⓞ orcid.org/0000-0002-6299-654X

Complete contact information is available at:
https://pubs.acs.org/10.1021/acsenergylett.3c01626

Notes

The authors declare no competing financial interest.

■ ACKNOWLEDGMENTS

■ REFERENCES

(1) Ferreira, K. N.; Iverson, T. M.; Maghlaoui, K.; Barber, J.; Iwata, S. Architecture of the Photosynthetic Oxygen-Evolving Center. *Science* **2004**, *303*, 1831−1838.

(2) Zhang, C.; Chen, C.; Dong, H.; Shen, J.-R.; Dau, H.; Zhao, J. A synthetic Mn_4Ca-cluster mimicking the oxygen-evolving center of photosynthesis. *Science* **2015**, *348*, 690−693.

(3) Yuan, S.; Peng, J.; Cai, B.; Huang, Z.; Garcia-Esparza, A. T.; Sokaras, D.; Zhang, Y.; Giordano, L.; Akkiraju, K.; Zhu, Y. G.; Hübner, R.; Zou, X.; Román-Leshkov, Y.; Shao-Horn, Y. Tunable metal hydroxide−organic frameworks for catalysing oxygen evolution. *Nat. Mater.* **2022**, *21*, 673−680.

(4) Umena, Y.; Kawakami, K.; Shen, J.-R.; Kamiya, N. Crystal structure of oxygen-evolving photosystem II at a resolution of 1.9 Å. *Nature* **2011**, *473*, 55−60.

(5) Kanady, J. S.; Lin, P.-H.; Carsch, K. M.; Nielsen, R. J.; Takase, M. K.; Goddard, W. A., III; Agapie, T. Toward Models for the Full Oxygen-Evolving Complex of Photosystem II by Ligand Coordination To Lower the Symmetry of the Mn_3CaO_4 Cubane: Demonstration That Electronic Effects Facilitate Binding of a Fifth Metal. *J. Am. Chem. Soc.* **2014**, *136*, 14373−14376.

(6) Tsui, E. Y.; Agapie, T. Reduction potentials of heterometallic manganese−oxido cubane complexes modulated by redox-inactive metals. *Proc. Natl. Acad. Sci. U. S. A.* **2013**, *110*, 10084−10088.

(7) Kärkäs, M. D.; Verho, O.; Johnston, E. V.; Åkermark, B. Artificial Photosynthesis: Molecular Systems for Catalytic Water Oxidation. *Chem. Rev.* **2014**, *114*, 11863−12001.

(8) Singh, M. R.; Bell, A. T. Design of an artificial photosynthetic system for production of alcohols in high concentration from CO_2. *Energy Environ. Sci.* **2016**, *9*, 193−199.

(9) Li, X.-B.; Tung, C.-H.; Wu, L.-Z. Semiconducting quantum dots for artificial photosynthesis. *Nat. Rev. Chem.* **2018**, *2*, 160−173.

(10) Dutta, U.; Maiti, S.; Bhattacharya, T.; Maiti, D. Arene diversification through distal C(sp^2)−H functionalization. *Science* **2021**, *372*, No. eabd5992.

(11) Suen, N.-T.; Hung, S.-F.; Quan, Q.; Zhang, N.; Xu, Y.-J.; Chen, H. M. Electrocatalysis for the oxygen evolution reaction: recent

development and future perspectives. *Chem. Soc. Rev.* **2017**, *46*, 337−365.

(12) Yocum, C. F. The calcium and chloride requirements of the O_2 evolving complex. *Coord. Chem. Rev.* **2008**, *252*, 296−305.

(13) Pecoraro, V. L.; Baldwin, M. J.; Caudle, M. T.; Hsieh, W. Y.; Law, N. A. A proposal for water oxidation in photosystem II. *Pure Appl. Chem.* **1998**, *70*, 925−929.

(14) Tsui, E. Y.; Tran, R.; Yano, J.; Agapie, T. Redox-inactive metals modulate the reduction potential in heterometallic manganese−oxido clusters. *Nat. Chem.* **2013**, *5*, 293−299.

(15) Xiao, H.; Shin, H.; Goddard, W. A. Synergy between Fe and Ni in the optimal performance of (Ni,Fe)OOH catalysts for the oxygen evolution reaction. *Proc. Natl. Acad. Sci. U. S. A.* **2018**, *115*, 5872−5877.

(16) Lee, Y.; Suntivich, J.; May, K. J.; Perry, E. E.; Shao-Horn, Y. Synthesis and Activities of Rutile IrO_2 and RuO_2 Nanoparticles for Oxygen Evolution in Acid and Alkaline Solutions. *J. Phys. Chem. Lett.* **2012**, *3*, 399−404.

(17) Lim, J.; Yang, S.; Kim, C.; Roh, C.-W.; Kwon, Y.; Kim, Y.-T.; Lee, H. Shaped Ir−Ni bimetallic nanoparticles for minimizing Ir utilization in oxygen evolution reaction. *Chem. Commun.* **2016**, *52*, 5641−5644.

(18) Olowoyo, J. O.; Kriek, R. J. Recent Progress on Bimetallic-Based Spinels as Electrocatalysts for the Oxygen Evolution Reaction. *Small* **2022**, *18*, No. 2203125.

(19) Grimaud, A.; Diaz-Morales, O.; Han, B.; Hong, W. T.; Lee, Y.-L.; Giordano, L.; Stoerzinger, K. A.; Koper, M. T. M.; Shao-Horn, Y. Activating lattice oxygen redox reactions in metal oxides to catalyse oxygen evolution. *Nat. Chem.* **2017**, *9*, 457−465.

(20) Suntivich, J.; Gasteiger, H. A.; Yabuuchi, N.; Nakanishi, H.; Goodenough, J. B.; Shao-Horn, Y. Design principles for oxygen-reduction activity on perovskite oxide catalysts for fuel cells and metal−air batteries. *Nat. Chem.* **2011**, *3*, 546−550.

(21) Li, S.; Chen, B.; Wang, Y.; Ye, M.-Y.; van Aken, P. A.; Cheng, C.; Thomas, A. Oxygen-evolving catalytic atoms on metal carbides. *Nat. Mater.* **2021**, *20*, 1240−1247.

(22) Buchwalter, P.; Rosé, J.; Braunstein, P. Multimetallic Catalysis Based on Heterometallic Complexes and Clusters. *Chem. Rev.* **2015**, *115*, 28−126.

(23) Liang, Q.; Chen, J.; Wang, F.; Li, Y. Transition metal-based metal-organic frameworks for oxygen evolution reaction. *Coord. Chem. Rev.* **2020**, *424*, No. 213488.

(24) Wang, H.-F.; Chen, L.; Pang, H.; Kaskel, S.; Xu, Q. MOF-derived electrocatalysts for oxygen reduction, oxygen evolution and hydrogen evolution reactions. *Chem. Soc. Rev.* **2020**, *49*, 1414−1448.

(25) Li, S.; Gao, Y.; Li, N.; Ge, L.; Bu, X.; Feng, P. Transition metal-based bimetallic MOFs and MOF-derived catalysts for electrochemical oxygen evolution reaction. *Energy Environ. Sci.* **2021**, *14*, 1897−1927.

(26) Zhou, Y.; Abazari, R.; Chen, J.; Tahir, M.; Kumar, A.; Ikreedeegh, R. R.; Rani, E.; Singh, H.; Kirillov, A. M. Bimetallic metal−organic frameworks and MOF-derived composites: Recent progress on electro- and photoelectrocatalytic applications. *Coord. Chem. Rev.* **2022**, *451*, No. 214264.

(27) Zhao, S.; Wang, Y.; Dong, J.; He, C.-T.; Yin, H.; An, P.; Zhao, K.; Zhang, X.; Gao, C.; Zhang, L.; Lv, J.; Wang, J.; Zhang, J.; Khattak, A. M.; Khan, N. A.; Wei, Z.; Zhang, J.; Liu, S.; Zhao, H.; Tang, Z. Ultrathin metal−organic framework nanosheets for electrocatalytic oxygen evolution. *Nat. Energy* **2016**, *1*, No. 16184.

(28) Hai, G.; Jia, X.; Zhang, K.; Liu, X.; Wu, Z.; Wang, G. High-performance oxygen evolution catalyst using two-dimensional ultra-thin metal-organic frameworks nanosheets. *Nano Energy* **2018**, *44*, 345−352.

(29) Hao, Y.; Liu, Q.; Zhou, Y.; Yuan, Z.; Fan, Y.; Ke, Z.; Su, C.-Y.; Li, G. A 2D NiFe Bimetallic Metal−Organic Frameworks for Efficient Oxygen Evolution Electrocatalysis. *Energy Environ. Mater.* **2019**, *2*, 18−21.

(30) Li, J.; Huang, W.; Wang, M.; Xi, S.; Meng, J.; Zhao, K.; Jin, J.; Xu, W.; Wang, Z.; Liu, X.; Chen, Q.; Xu, L.; Liao, X.; Jiang, Y.; Owusu, K. A.; Jiang, B.; Chen, C.; Fan, D.; Zhou, L.; Mai, L. Low-Crystalline Bimetallic Metal−Organic Framework Electrocatalysts with Rich Active Sites for Oxygen Evolution. *ACS Energy Lett.* **2019**, *4*, 285−292.

(31) Zhang, M.; Xu, W.; Li, T.; Zhu, H.; Zheng, Y. In Situ Growth of Tetrametallic FeCoMnNi-MOF-74 on Nickel Foam as Efficient Bifunctional Electrocatalysts for the Evolution Reaction of Oxygen and Hydrogen. *Inorg. Chem.* **2020**, *59*, 15467−15477.

(32) Clérac, R.; O'Kane, S.; Cowen, J.; Ouyang, X.; Heintz, R.; Zhao, H.; Bazile, M. J.; Dunbar, K. R. Glassy Magnets Composed of Metals Coordinated to 7,7,8,8-tetracyanoquinodimethane: M-$(TCNQ)_2$ (M = Mn, Fe, Co, Ni). *Chem. Mater.* **2003**, *15*, 1840−1850.

(33) Tseng, T.-C.; Urban, C.; Wang, Y.; Otero, R.; Tait, S. L.; Alcamí, M.; Écija, D.; Trelka, M.; Gallego, J. M.; Lin, N.; Konuma, M.; Starke, U.; Nefedov, A.; Langner, A.; Wöll, C.; Herranz, M. Á.; Martín, F.; Martín, N.; Kern, K.; Miranda, R. Charge-transfer-induced structural rearrangements at both sides of organic/metal interfaces. *Nat. Chem.* **2010**, *2*, 374−379.

(34) Kamitsos, E. I.; Risen, W. M., Jr. Raman studies in CuTCNQ: Resonance Raman spectral observations and calculations for TCNQ ion radicals. *J. Chem. Phys.* **1983**, *79*, 5808−5819.

(35) Zhao, H.; Heintz, R. A.; Ouyang, X.; Dunbar, K. R.; Campana, C. F.; Rogers, R. D. Spectroscopic, Thermal, and Magnetic Properties of Metal/TCNQ Network Polymers with Extensive Supramolecular Interactions between Layers. *Chem. Mater.* **1999**, *11*, 736−746.

(36) Dhara, B.; Jha, P. K.; Gupta, K.; Bind, V. K.; Ballav, N. Diamagnetic Molecules Exhibiting Room-Temperature Ferromagnetism in Supramolecular Aggregates. *J. Phys. Chem. C* **2017**, *121*, 12159−12167.

(37) Blöchl, P. E. Projector augmented-wave method. *Phys. Rev. B* **1994**, *50*, 17953−17979.

(38) Perdew, J. P.; Burke, K.; Ernzerhof, M. Generalized Gradient Approximation Made Simple. *Phys. Rev. Lett.* **1996**, *77*, 3865−3868.

(39) Kresse, G.; Joubert, D. From ultrasoft pseudopotentials to the projector augmented-wave method. *Phys. Rev. B* **1999**, *59*, 1758−1775.

(40) Guo, X.; Zhu, S.; Kong, R.-M.; Zhang, X.; Qu, F. Fe$(TCNQ)_2$ Nanorod Array: A Conductive Non-Noble-Metal Electrocatalyst toward Water Oxidation in Alkaline Media. *ACS Sustain. Chem. Eng.* **2018**, *6*, 1545−1549.

(41) Xie, M.; Xiong, X.; Yang, L.; Shi, X.; Asiri, A. M.; Sun, X. An Fe$(TCNQ)_2$ nanowire array on Fe foil: an efficient non-noble-metal catalyst for the oxygen evolution reaction in alkaline media. *Chem. Commun.* **2018**, *54*, 2300−2303.

(42) Guo, X.; Kong, R.-M.; Zhang, X.; Du, H.; Qu, F. Ni$(OH)_2$ Nanoparticles Embedded in Conductive Microrod Array: An Efficient and Durable Electrocatalyst for Alkaline Oxygen Evolution Reaction. *ACS Catal.* **2018**, *8*, 651−655.

(43) Wei, Y.; Ren, X.; Ma, H.; Sun, X.; Zhang, Y.; Kuang, X.; Yan, T.; Wu, D.; Wei, Q. In situ Formed Co$(TCNQ)_2$ Metal-Organic Framework Array as a High-Efficiency Catalyst for Oxygen Evolution Reactions. *Chem.—Eur. J.* **2018**, *24*, 2075−2079.

(44) Wu, D.; Wei, Y.; Ren, X.; Ji, X.; Liu, Y.; Guo, X.; Liu, Z.; Asiri, A. M.; Wei, Q.; Sun, X. Co$(OH)_2$ Nanoparticle-Encapsulating Conductive Nanowires Array: Room-Temperature Electrochemical Preparation for High-Performance Water Oxidation Electrocatalysis. *Adv. Mater.* **2018**, *30*, No. 1705366.

(45) Ren, X.; Ji, X.; Wei, Y.; Wu, D.; Zhang, Y.; Ma, M.; Liu, Z.; Asiri, A. M.; Wei, Q.; Sun, X. In situ electrochemical development of copper oxide nanocatalysts within a TCNQ nanowire array: a highly conductive electrocatalyst for the oxygen evolution reaction. *Chem. Commun.* **2018**, *54*, 1425−1428.

(46) Liu, L.; Wu, Q.; Guo, H.; Li, L.; Liu, M.; Li, D.; Wang, H.; Chen, L. Mn$(TCNQ)_2$ nanorod array on copper foam: A high-performance and conductive electrocatalyst for oxygen evolution reaction. *Mater. Lett.* **2018**, *230*, 53−56.

(47) Zhu, X.; Shi, X.; Asiri, A. M.; Luo, Y.; Sun, X. Efficient oxygen evolution electrocatalyzed by a Cu nanoparticle-embedded N-doped carbon nanowire array. *Inorg. Chem. Front.* **2018**, *5*, 1188−1192.

(48) Li, W.-H.; Lv, J.; Li, Q.; Xie, J.; Ogiwara, N.; Huang, Y.; Jiang, H.; Kitagawa, H.; Xu, G.; Wang, Y. Conductive metal−organic framework nanowire arrays for electrocatalytic oxygen evolution. *J. Mater. Chem. A* **2019**, *7*, 10431−10438.

(49) Wan, Z.; Yang, D.; Chen, J.; Tian, J.; Isimjan, T. T.; Yang, X. Oxygen-Evolution Catalysts Based on Iron-Mediated Nickel Metal−Organic Frameworks. *ACS Appl. Nano Mater.* **2019**, *2*, 6334−6342.

(50) Louie, M. W.; Bell, A. T. An Investigation of Thin-Film Ni−Fe Oxide Catalysts for the Electrochemical Evolution of Oxygen. *J. Am. Chem. Soc.* **2013**, *135*, 12329−12337.

(51) Chen, F.-Y.; Wu, Z.-Y.; Adler, Z.; Wang, H. Stability challenges of electrocatalytic oxygen evolution reaction: From mechanistic understanding to reactor design. *Joule* **2021**, *5*, 1704−1731.

(52) Bendavid, L. I.; Carter, E. A. CO_2 Adsorption on Cu_2O(111): A DFT+U and DFT-D Study. *J. Phys. Chem. C* **2013**, *117*, 26048−26059.

(53) Jin, S. Are Metal Chalcogenides, Nitrides, and Phosphides Oxygen Evolution Catalysts or Bifunctional Catalysts? *ACS Energy Lett.* **2017**, *2*, 1937−1938.

(54) Zhao, S.; Tan, C.; He, C.-T.; An, P.; Xie, F.; Jiang, S.; Zhu, Y.; Wu, K.-H.; Zhang, B.; Li, H.; Zhang, J.; Chen, Y.; Liu, S.; Dong, J.; Tang, Z. Structural transformation of highly active metal−organic framework electrocatalysts during the oxygen evolution reaction. *Nat. Energy* **2020**, *5*, 881−890.

(55) Zheng, W.; Liu, M.; Lee, L. Y. S. Electrochemical Instability of Metal−Organic Frameworks: In Situ Spectroelectrochemical Investigation of the Real Active Sites. *ACS Catal.* **2020**, *10*, 81−92.

(56) Mabayoje, O.; Shoola, A.; Wygant, B. R.; Mullins, C. B. The Role of Anions in Metal Chalcogenide Oxygen Evolution Catalysis: Electrodeposited Thin Films of Nickel Sulfide as "Pre-catalysts. *ACS Energy Lett.* **2016**, *1*, 195−201.